Sustainable Energy & Fuels

Interdisciplinary research for the development of sustainable energy technologies

Accepted Manuscript

This article can be cited before page numbers have been issued, to do this please use: A. Abioro, O. Astakhov, S. Schecherbanchenko, C. Ampelli, D. Giusi, G. Centi, S. Perathoner, E. Neumann, Y. J. Sohn, C. J. Brabec and T. Merdzhanova, *Sustainable Energy Fuels*, 2026, DOI: 10.1039/D6SE00442C.

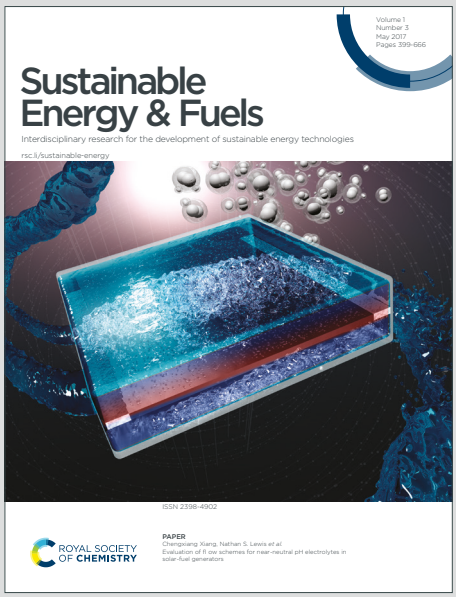

View Article Online
DOI: 10.1039/D6SE00442C

From sunlight to formate at realistic temperatures and dynamic irradiance: direct photovoltaic–electrochemical CO_2 reduction using a Cu_2O:S gas diffusion electrode

Ameerah Abioro[a], Oleksandr Astakhov[a], Sergey Schecherbanchenko[a], Claudio Ampelli[b], Daniele Giusi[b], Gabriele Centi[b], Siglinda Perathoner[b], Elmar Neumann[c], Yoo Jung Sohn[d], Christoph J. Brabec[a], Tsvetelina Merdzhanova[a]

[a] Ameerah Abioro, Oleksandr Astakhov, Sergey Schecherbanchenko, Christoph J. Brabec, Tsvetelina Merdzhanova
Photovoltaik (IMD-3)
Forschungszentrum Jülich GmbH, 52425 Jülich, Germany
E-mail: t.merdzhanova@fz-juelich.de

[b] Claudio Ampelli, Daniele Giusi, Gabriele Centi, Siglinda Perathoner
Department of Chemical, Biological, Pharmaceutical and Environmental Sciences (ChiBioFarAm)
University of Messina, ERIC aisbl and CASPE/INSTM
Messina, Italy

[c] Elmar Neumann
Helmholtz Nano Facility (HNF)
Forschungszentrum Jülich, 52425 Jülich, Germany

[d] Yoo Jung Sohn
Institute of Energy Materials and Devices IMD-2
Forschungszentrum Jülich GmbH, 52425 Jülich, Germany

Abstract: Solar-driven CO_2 reduction to liquid fuels such as formate provides an attractive solution for renewable energy storage. This paper investigates the application of an electrochemical (EC) cell for CO_2 reduction directly coupled to a photovoltaic (PV) module, which enables early-stage, long-term storage of solar energy through a waste-to-value pathway. An earth-abundant gas-diffusion cathode based on sulfur-modified copper oxide is employed as the core catalyst for the CO_2 reduction process. The cathode is synthesized and tested in a gas-diffusion electrode (GDE) flow-cell configuration under conditions of a realistic, directly coupled PV-EC device. Realistic field operation of the PV-EC device is reproduced using a hardware PV emulator replicating the Si PV module *I-V* characteristics over a full day–night irradiance and temperature time series, while EC cell operates at 40 °C. Under these realistic operating conditions, the directly coupled PV-EC device demonstrates self-sustained operation with a high energy-coupling efficiency of 94%. The sulfur-modified copper oxide catalyst achieves stable CO_2 reduction with a total solar-to-chemical efficiency of ~12% and a solar-to-formate efficiency (STC_{HCOO^-}) of ~8% at current densities of 6 - 19 mA cm^{-2}. Our achieved STC_{HCOO^-} is presented alongside recorded operating current densities (j_{OP}) against previously reported literature, allowing for direct comparison between different electrochemical catalysts, cell designs or coupling strategies. Our results demonstrate the feasibility of liquid-fuel production under realistic PV-driven direct-coupling operation, representing a key step toward

View Article Online
DOI: 10.1039/D6SE00442C

early-stage long-term storage of surplus PV output in renewable-energy-dominated systems, and coupling of PV generation to non-electrified energy sectors.

Introduction

CO_2 as a greenhouse gas propagates infrared re-emission, leading to gross negative environmental and climate changes.[1–3] This is the driving force behind advancements in the mitigation of the atmospheric accumulation of CO_2, whereby a number of approaches are considered, including CO_2 usage, storage, and the reduction of the amount of CO_2 produced by using low- or non-carbon technologies and energy sources.[2–6] In 2024, global CO_2 emissions from energy combustion and industrial processes increased by approximately 3.6% in comparison to pre-pandemic levels.[7] Transition of electricity generation to renewable energy sources belongs to major measures of reducing CO_2 emissions. The deployment of solar photovoltaic (PV) alone curtailing around 1.4 Gt of annual CO_2 emissions worldwide.[7] At the same time, variability and intermittency of PV generation stand in the way of fast PV deployment toward large energy shares due to the natural generation-demand mismatch.[8–12] This temporal generation-demand mismatch can be resolved by temporal PV energy coupling to the load via energy storage. This storage must cover essentially two timescales: the relatively short time scale from weather related fluctuations to daily variations and the long-time seasonal variations of PV output. Most versatile scalable and universal storage solutions belong to the realm of electrochemical devices. The short time scale management involves PV coupling to supercapacitors[13–16] and batteries[17–19] while seasonality is addressed with electrolyzers[20–23] producing fuels and chemicals. The whole required timescale can be covered via hybrid systems[24–28]. The electrochemical route for the long term storage has additional advantage as it can utilize CO_2 as a feedstock for solar fuel production via the electrochemical CO_2 reduction.[29–31] The storage in general and particularly electrochemical (EC) CO_2 reduction can be coupled to PV at different stages of electricity conversion and transmission. In order to minimize the overhead for the grid reinforcement, the PV variability must be captured as close to the origin as possible. The ultimate solution is to couple storage at the PV module or PV string level directly without any intermediate power conversion or conditioning. The feasibility and high performance of direct coupled PV-EC devices particularly for CO_2 reduction have been reported in numerous studies.[32–34] These studies however mostly address constant standard lab conditions well suited for accurate performance evaluation but less indicative for the validity of the approach for field applications. This gap has to be covered in order to increase technology readiness level of the promising PV-EC CO_2 reduction solutions. Testing the PV-EC approach in realistic operating cycle is one of the main goals of this work. Another aspect of the close coupling of PV and EC is the practicality of product handling. In the case of the distributed EC storage solution, it is highly desirable to produce liquid products which simplifies and reduces cost of product collection and handling. In this work we address both aspects by testing EC cell producing formate ($HCOO^-$) in direct coupling to the PV device exposed to realistic daily operating cycles. On the EC side the operating temperature has been elevated to 40 °C in order to approach conditions typical for industrial low temperature electrolyzers. Any EC technology developed as storage solution for

View Article Online
DOI: 10.1039/D6SE00442C

PV must be scalable up to TW scale, which implies it must be based on abundant materials. We approach this key aspect of the development by testing an earth-abundant gas diffusion cathode that is based on sulfur-modified copper oxide. With appropriate formulation, particularly low S content, these catalyst components enhance selectivity to formate and reduce the formation of CO, allowing for a high carbon selectivity[35–37]. To facilitate the cathode reaction, the sulfur-modified copper oxide was airbrushed on a gas diffusion layer (GDL) substrate (Cu_2O:S/GDL). The focus of the work was on the cathode side performance and therefore, established IrO_2/GDL was used on the anode side for water oxidation in the oxygen evolution reaction (OER). For the PV-power input, a Si-based PV module with an efficiency of 24.8% (Standard Test Conditions (STC): AM 1.5 1000 W m^{-2} 25 °C) was used. One key limitation of typical PV-EC experiments is mismatching the device sizes and voltages. The lab scale electrochemical devices have geometrical electrode areas from few cm^2 to approx. hundred cm^2 and are represented by single cell reactor. Operating voltage of such devices ranges typically 2…5 V with power of 0.1…10 W. The practically relevant commercial PV modules include 60 or more cells power of hundreds of Watts. Therefore, the PV-EC experiments must rely on small size custom PV devices which are less representative for real field applications and severely limit flexibility and finetuning of the PV-EC devices. Another experimental limitation is related to the difficulties in realizing long term experiments with variable irradiance and temperature for the PV devices. To overcome these limitations we employ our recently developed PV emulator[38] which is capable to reproduce the physical *I-V* output of any required PV module under the target timeseries of temperature and irradiance, and successfully applied in our previous works.[39–41] The emulator provides flexibility in the choice of PV module the timeseries of PV conditions and scaling of the PV output to match the EC operating range. With this approach we can test an EC device of any scale as if it was a part of the real PV-EC device configuration operating under the target climatic conditions and reproduce the experiment with high accuracy for required number of times. Here, the operating profile of the PV module was represented by a typical sunny summer day in Freiburg, Germany over various plane-of-array (POA) irradiances (*G*) and PV module temperatures (*T*), depicting sunrise to sunset.

The PV-EC device demonstrated stable operation under the investigated fluctuating input power conditions, with high energy coupling efficiency achieved between the two devices and improved *I-V* characteristics of the EC cell observed thereafter. The fabricated cathode material retained its overall selectivity to formate under these operating conditions and showed no major irreversible loss of catalytic activity via linear sweep voltammetry (LSV) after over 6 hours of PV-EC device operation and electrolyte replacement. This work provides an introduction for scalable, real-world outdoor applications of direct coupled PV-EC device configurations, whereby highly efficient solar fuel production can be designed and tuned through optimized coupling of the devices. This is a key step toward early-stage long-term storage of surplus PV output in renewable-energy-dominated systems, and coupling of PV generation to non-electrified energy sectors.

The paper is organized as follows:

First, the experimental details of the materials, measurement procedures, and testing setup are presented, including the experimental preparation and characterization of materials. Then, the devices utilized in the

View Article Online
DOI: 10.1039/D6SE00442C

PV-EC configuration are described, alongside relevant optimization techniques, total performance evaluation and key performance metrics used for assessment. Subsequently, the properties of the synthesized cathode material are discussed, and its temperature- and voltage-dependent performance in the EC cell is evaluated across a cell voltage range of 2.4 V to 3.2 V and a temperature range of 20 °C to 60 °C. Finally, the PV-EC configuration is tested in a realistic day cycle under the target climatic conditions using a PV emulator. The results are shown and discussed individually and in comparison with previously reported literature in terms of STC_{HCOO^-} and j_{OP}.

Experimental

Solvothermal synthesis of Cu_2O:S catalyst

16 mmol of copper(II) nitrate trihydrate (Sigma-Aldrich ≥ 99.5%) was homogenized in 80 mL of ethylene glycol (Sigma-Aldrich ≥ 99%) for 30 minutes at room temperature. The mixture was then transferred into a 125 mL polytetrafluoroethylene (PTFE) cup where 0.268 mmol of elemental sulfur flake (Sigma-Aldrich 99.998%) was broken into smaller particle sizes. The PTFE cup was then heat treated at 140 °C in an autoclave, with an initial ramp rate of 5 °Cmin^{-1} for 10 h and then allowed to naturally cool to room temperature. The resulting mixture was washed by centrifugation with Milli-Q water (18 MΩ·cm) at 4000 rpm for 10 min in three cycles. The powder obtained was dried overnight in the oven at 80 °C. The representative schematic is shown in **Figure S1a**.

Fabrication of gas diffusion electrodes

Gas diffusion layer (GDL) sheets (Ion Power, Sigracet 39BB) were used as substrates for both gas diffusion electrodes (GDEs). A 36 mm diameter hole punch (JLB 260PACC, BOEHM) was used to cut the substrate material into the desired shape. The cathode and anode were fabricated using the synthesized Cu_2O:S powder and commercially purchased IrO_2 (Thermo Scientific, 99.99% metal basis) powder, respectively. For each electrode, 100 mg catalyst powder, 100 µL Nafion 117 (Sigma-Aldrich, 5 wt% in a mixture of lower aliphatic alcohols and water) and 4 mL 2-propanol (VWR Chemicals, ≥ 98%) were combined to form a catalyst ink. The inks were then ultrasonicated for at least 30 min at room temperature before being sprayed onto the GDL with an airbrush (Iwata Eclipse Takumi) supported on a hot plate at 40 °C to facilitate solvent evaporation. A mold was applied such that only a diameter of 30 mm was airbrushed and then the amount of catalyst loading in mg cm^{-2} for each electrode was determined by comparing the weight of the bare substrate and gas diffusion electrode (GDE), with a targeted catalyst load of 1.5 mg cm^{-2}. The representative schematic is shown in **Figure S1b**.

Surface characterization of cathode material

The synthesized Cu_2O:S powder was analyzed via X-ray diffraction (XRD) using Empyrean (Malvern Panalytical, Netherlands) to evaluate its crystal structure. The patterns were recorded in the 20–80° 2θ

View Article Online
DOI: 10.1039/D6SE00442C

range with a step size of 0.026° and a counting time of 250 s per step using a 255 channel PIXcel detector. The morphology and composition of the self-prepared Cu_2O:S/GDL was characterized before use via scanning electron microscopy (SEM) and energy dispersive X-ray spectroscopy (EDX), employing the FEI Magellan in combination with a conversion tool, EDX detector model X-Max 80 mm^2 (Oxford Instruments GmbH) and the respective software (AZtec 6.1).

Electrochemical CO_2 reduction setup

A custom-built GDE flow cell consisting of a cathode side, anode side and gas chamber was used for the electrochemical CO_2 reduction reactions. A visual representation of the EC cell and its components is shown in **Figure 1**. The EC cell gas chamber was integrated on the cathode side and separated from it by the gas diffusion cathode/working electrode, while the cathode and anode sides were separated by a PTFE reinforced cation exchange membrane (N324, Nafion). The in-house-prepared Cu_2O:S/GDL and IrO_2/GDL with a diameter of 36 mm were employed as the cathode and anode, respectively. 0.1M $KHCO_3$ saturated with CO_2 at a flow rate of 20 sccm was used as the catholyte, whilst 1M KOH was used as the anolyte. Both electrolytes flowed from their respective reservoirs into the EC cell at a flow rate of 50 rpm. CO_2 gas was also introduced into the EC cell via the gas chamber inlet at 20 sccm as shown in the representative schematic below. With the gas chamber outlet on the GDE flow cell closed, only the overhead space in the cathode reservoir was investigated for gaseous products using an online gas chromatograph. The full schematic of the experimental set-up is depicted in **Figure S2.**

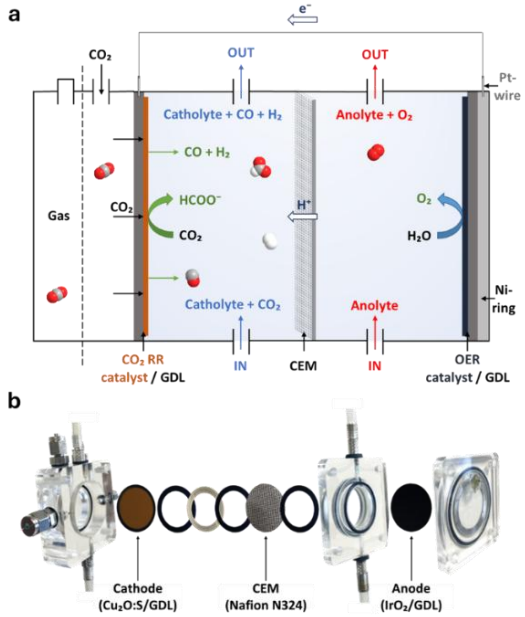

Figure 1. Visual representation of the gas diffusion electrode (GDE) flow cell used and its components. **a** Schematic illustration of the working principle of the electrochemical (EC) cell. The abbreviations 'GDL', 'CO_2RR', 'CEM', and 'OER' correspond to gas diffusion layer, carbon dioxide reduction reaction, cation

View Article Online
DOI: 10.1039/D6SE00442C

exchange membrane, and oxygen evolution reaction, respectively. **b** Exploded view of the EC cell showing related electrodes, membrane and sealing gaskets.

Ambient pressure electrolysis was performed in a two-electrode configuration between 20 °C and 60 °C at an applied cell voltage of 2.6 V and at 40 °C at a cell voltage range of 2.4 V to 3.2 V. In both cases, the electrolytes were heated using heating pipes along the tubing and the temperature was monitored using a temperature controller connected to the electrolyte reservoirs. Linear sweep voltammetry (LSV) measurements were also performed periodically to explore the electrochemical behavior of the cathode material. Measurements for the electrochemical characterization of the EC cell were performed at temperatures between 20 °C and 60 °C using the multichannel OrigaFlex potentiostat (OGFDRV and OGF05A, OrigaLys). At each operating temperature, an LSV was measured at a scan rate of 5 mV s^{-1} followed by a CA measurement at an applied voltage of 2.6 V for a time period of 1 h. After each LSV and CA run, the used electrolytes were flushed, and a new batch of fresh electrolytes were introduced into the EC cell before being heated up to the required temperature for the next measurement. For the target operation of the EC cell with a PV device, the experiments were performed at 40 °C using a PV emulator. Here, the same electrolytes were used throughout, with a 15 min rest period observed between applied voltages.

PV emulation

A PV emulator has been applied to provide realistic output of a commercial PV module installed in Freiburg, Germany. The PV emulator is designed to accurately reproduce the electric output of the target PV module according to its IV under the target operating conditions. The emulator consists of both hardware (PC and source measure unit) and software components (Python and Standard Commands for Programmable Instruments (SCPI)).[38] Application of the PV emulator allows to couple output of realistic PV device installed in the field to the experimental EC devices operating in a typical electrochemical lab with necessary scaling and mutual matching to realize conditions of properly designed PV-EC device. This enables operation under defined irradiance and temperature conditions in accurately controlled and reproducible experiments and flexible selection of PV module (type, size, and number of cells) as demonstrated in our previous studies[38–41].

In this work, the output of AIKO-A495-MCE54Mw Si-based PV module from Neostar was used for emulation. Its parameters are described in the Supplementary Information. Initially, all current–voltage (*I-V*) curves are generated for the reference PV module for a typical sunny summer day in Freiburg, Germany using standard six-parameter photovoltaic module model (CEC6PPVMM[42]) as described in the Supplementary Information. The generated PV module *I-V* curves over the representative 24-hour condition set are shown in **Figure S3**. We selected a temporal subset (hours 5-22) of the original set for the operating profile and then derived a condensed (accelerated) laboratory timescale of around 7 hours from it. While this timescale enables direct comparison with existing literature, it does not yet reflect the long-term operational stability required for practical applications. The profile features plane-of-array irradiance (*G*) from 36 W m^{-2} to a

View Article Online
DOI: 10.1039/D6SE00442C

maximum of 1055 W m^{-2} and back to 8 W m^{-2}, and PV module temperatures (T) from 4 °C at the beginning of the day, 42 °C at maximum solar irradiance, and 13 °C at the end of day. All combinations of G and T in the original 24-hour set, and condensed laboratory timescale are shown in **Figure S4**. The original PV module has an active area of approximately 2 m^2 and consists of $N_{S,mod}$ = 54 cells connected in series which results in severe output voltage and current mismatch to the tested lab scale EC device.

For proper function and optimal performance, the elements of the PV-EC device must be power-matched. This is achieved via selection and scaling of the PV and EC parts in such a way that the common operating point at the intersection of their *I-V* characteristics is at or close to the maximum power point of the PV module and is within the target operating range of the EC device. The PV emulation approach provides useful flexibility in this case as the PV *I-V* can be scaled to match the lab scale EC. The PV *I-V* scaling along the voltage axis in practical terms is equivalent to the selection of such number of PV and EC cells connected in series in PV and EC modules, respectively, to match the required voltage. The scaling of the PV current or power is equivalent to the scaling of the area of PV or EC device. The PV module voltage V_{mod} is a product of the cell voltage V_{cell} and the number of cells connected in series N_S. Optimal output of the PV module is attained at the maximum power point voltage V_{mpp_mod} therefore we use this voltage for scaling. EC device voltage follows trivially the same rule while the target operating voltage is defined by the optimal performance and product evolution. Once the EC target voltage V_{EC_target} is specified the voltage adjustment of PV *I-V* is done by multiplying the *I-V* by the following scaling factor

$$v_{\text{scaling}} = \frac{V_{\text{EC}}\, N_{\text{cEC}}}{V_{\text{mpp}}\, N_{\text{cPV}}} \tag{1}$$

Where $v_{scaling}$ is the factor for scaling the PV *I-V* along the voltage axis. V_{EC} is the target operating voltage for the single EC cell, N_{cEC} is the number of EC cells connected in series, V_{mpp} is the maximum power point of the single PV cell under reference operating conditions and N_{cPV} is the number of PV cells in series.

The scaling along the current scale is related to current densities of the devices and their areas as follows

$$i_{\text{scaling}} = \frac{j_{\text{EC}}\, A_{\text{EC}}}{j_{\text{mpp}}\, A_{\text{PV}}} \tag{2}$$

Where $i_{scaling}$ is the factor for scaling the PV *I-V* along the current axis. j_{EC} is the target operating current density of the EC cell, A_{EC} is the area of the EC cell, j_{mpp} is the maximum power point current density of the whole PV device calculated as the total current of the PV cell or module divided by its total area A_{PV}.

Using these scaling factors the generated set of the PV *I-V* curves are converted into the resulting set of *I-V*s shown in **Figure 2a** prepared to drive the EC cell in our experiment. In a direct coupled PV-EC configuration, the operating current and voltage (I_{OP} and V_{OP}) at the intersection of the PV *I-V* curve and the EC polarization curve determine the electric PV output and EC input, respectively,[43–45] where operating power is $P_{OP} = V_{OP} \times I_{OP}$. Note that the scaling of PV device is naturally done once, at the PV-EC design

View Article Online
DOI: 10.1039/D6SE00442C

phase. At the same time, variety of the ambient conditions makes the choice of the scaling factors less obvious as compared to the typical laboratory standard test conditions. Optimization of the scaling in realistic scenario can be performed with aim to optimize the system efficiency towards the target product. This optimization requires simulation of the system output for the whole timeseries of the test scenario and calculation of the product output based on the EC characteristics. By scanning over the range of PV voltage and current scaling the optimum can be found. The optimization is performed for formate ($HCOO^-$) and the solar-to-formate efficiency as the optimization criterion. The results of these optimizations are shown in **Figure 2b**.

The voltage efficiency of the EC cell for a specific reaction product at the operating point is defined as

$$\eta_{\text{voltage,i}}(V_{\text{OP}}) = \frac{E^{\circ}_{\text{i}}}{V_{\text{OP}}} \tag{3}$$

Where E°_{i} is the theoretical thermodynamic potential required for the formation of a specific electrochemical reaction product and V_{OP} is the operating cell voltage of the EC cell. E° for $HCOO^-$ is 1.43 V. The Faradaic efficiency for formate FE_{HCOO^-} is determined experimentally by comparing the charge corresponding to formate production with the total charge after a time period as shown in **Eq.** (S1)**.** The instantaneous power contributing to formate production is therefore given by

$$P_{\text{HCOO}^-}(t) = P_{\text{OP}}(t) \times \eta_{\text{voltage}}(V_{\text{OP}}) \times FE_{\text{HCOO}^-} \tag{4}$$

As temperature and irradiance vary according to the prescribed operating reference profile, this power is calculated at each time step. Integration of $P_{HCOO^-}(t)$ over time gives the total energy predicted to be converted into formate production. The solar-to-formate efficiency (STC_{HCOO^-}) is then obtained as

$$STC_{\text{HCOO}^-} = \frac{\int P_{\text{HCOO}^-}(t)\, dt}{\int G(t) \times A_{\text{target}}\, dt} \tag{5}$$

Where $G(t)$ is the incident solar irradiance [W m^{-2}] and A_{target} is the active area of the PV module [m^2].

View Article Online
DOI: 10.1039/D6SE00442C

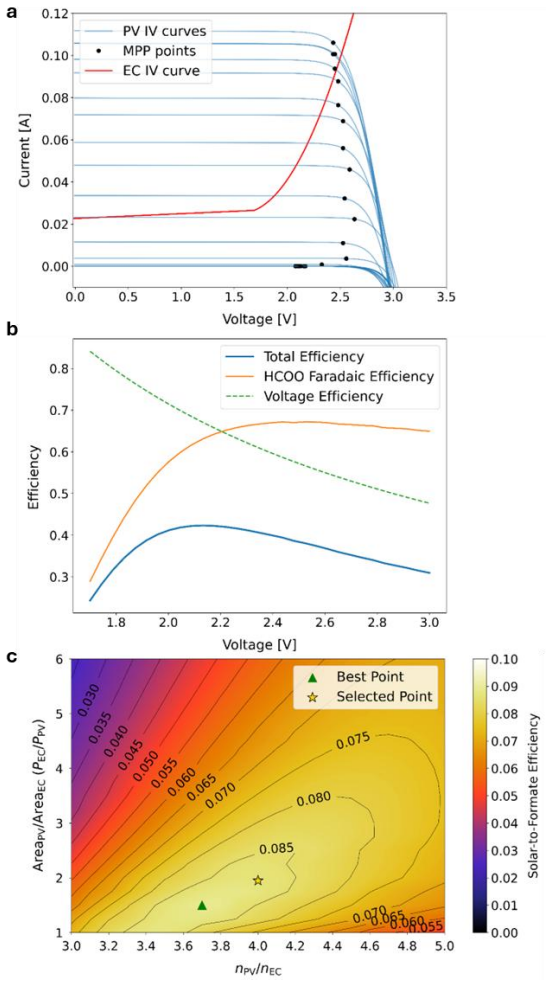

Figure 2. PV–EC configuration performance evaluation. **a** Polarization curve of the EC cell plotted together with the family of scaled PV module *I-V* curves over the representative 24-hour condition set. Blue curves represent PV *I-V* characteristics at each hour, black markers denote the corresponding MPP points, and the red curve is the EC *I-V*. **b** Calculated EC efficiency as a function of operating voltage, showing voltage efficiency (green), Faradaic efficiency toward formate (orange), and total solar-to-formate efficiency (blue) which is a product of both. **c** Solar-to-formate efficiency map as a function of the PV and EC cell-number ratio (η_{PV}/η_{EC}) and the PV-to-EC area ratio (A_{PV}/A_{EC}). Contours indicate efficiency levels, with the global maximum marked by a green triangle and the selected design point marked by a golden star.

By repeating this calculation for different values of $N_{S,target}$ and A_{target}, and expressing the results as a function of the PV-to-EC area ratio, one obtains a PV-EC device matching map as shown in **Figure 2c**, which visualizes the optimal coupling conditions between the photovoltaic and electrochemical components. Note that the x and y scales are presented by the ratios of PV and EC cell numbers (η_{PV}/η_{EC}) and PV-to-EC areas (A_{PV}/A_{EC}) to link the optimization to the physical properties of both devices. **Figure 2c** shows the predicted solar-to-formate efficiency (STC_{HCOO^-}) global maximum marked by a green triangle, and the

View Article Online
DOI: 10.1039/D6SE00442C

selected design point, marked by a golden star. This selected design point corresponds to higher values for both η_{PV}/η_{EC} and A_{PV}/A_{EC}. A higher PV-to-EC area ratio accounts for better operating conditions for power input without limited operation of the EC cell below the onset voltage of the target product, particularly under dynamic solar irradiance, showing a trade-off between theoretical maximum performance for STC_{HCOO^-} and practical operability.

Metrics for performance evaluation of PV-EC device

To evaluate the performance of the PV-EC device, the solar-to-chemical efficiency (*STC*) of the produced chemicals are calculated as follows

$$STC_{\mathrm{i}} = \eta_{\mathrm{PV}} \times C_{\mathrm{PV-EC}} \times \eta_{\mathrm{EC,i}} \tag{6}$$

where η_{PV} is the PV efficiency, $C_{PV\text{-}EC}$ is the PV-EC coupling efficiency and $\eta_{EC,i}$ is the efficiency of the EC cell in the formation of a specific reaction product. *STC* shows the efficiency of solar energy conversion in the production of chemicals.[45] The PV efficiency is defined as the ratio of the electrical energy delivered by the PV device at its maximum power point (MPP) to the incident solar energy received by the device over a given time interval. Both quantities are obtained by integrating power with respect to time.

$$\eta_{\mathrm{PV}} = \frac{E_{\mathrm{MPP}}}{E_{\mathrm{Sun}}} = \frac{\int_{t_1}^{t_2} P_{\mathrm{MPP}}(t)\,dt}{\int_{t_1}^{t_2} G(t) \times A_{\mathrm{PV}}\,dt} = \frac{\int_{t_1}^{t_2} \left(I_{\mathrm{MPP}}(t) \times V_{\mathrm{MPP}}(t)\right) dt}{\int_{t_1}^{t_2} G(t) \times A_{\mathrm{PV}}\,dt} \tag{7}$$

The electrical power at maximum power point P_{MPP}, is the product of the current and voltage at maximum power point, I_{MPP} and V_{MPP}. The total incident solar power E_{Sun} is the product of the solar irradiance *G(t)* and area of the PV device A_{PV}. η_{PV} is a measure of how much of the incident solar irradiation reaching the surface of the PV device is converted into the PV electrical power at maximum power point.

The energy coupling efficiency $C_{PV\text{-}EC}$ is defined as the ratio of the total energy utilized by the EC cell to the maximum deliverable energy by the PV device over a given time interval. This metric is used to evaluate how effectively the PV device and EC cell are matched in a direct coupled system.

$$C_{\mathrm{PV-EC}} = \frac{E_{\mathrm{OP}}}{E_{\mathrm{MPP}}} = \frac{\int_{t_1}^{t_2} P_{\mathrm{OP}}(t)\,dt}{\int_{t_1}^{t_2} P_{\mathrm{MPP}}(t)\,dt} = \frac{\int_{t_1}^{t_2} \left(I_{\mathrm{OP}}(t) \times V_{\mathrm{OP}}(t)\right) dt}{\int_{t_1}^{t_2} \left(I_{\mathrm{MPP}}(t) \times V_{\mathrm{MPP}}(t)\right) dt} \tag{8}$$

The power coupling factor is defined as the ratio of the instantaneous power utilized by the EC cell at operating point to the maximum deliverable power by the PV device at MPP. The electrical power at the operating point of the EC cell P_{OP}, is the product of the operating current I_{OP} and operating voltage V_{OP}.

$$C = \frac{P_{\mathrm{OP}}}{P_{\mathrm{MPP}}} = \frac{I_{\mathrm{OP}} \times V_{\mathrm{OP}}}{I_{\mathrm{MPP}} \times V_{\mathrm{MPP}}} \tag{9}$$

View Article Online
DOI: 10.1039/D6SE00442C

For a defined operating point, $\eta_{EC,i}$ is generally defined as the product of the Faradaic efficiency and the voltage efficiency of said reaction product as given in **Eq.** $(S1)$ and **Eq.** (3), respectively. The theoretical thermodynamic potential $E°$ for $HCOO^-$, H_2 and CO are 1.43 V, 1.23 V and 1.34 V, respectively.

$$\eta_{EC,i} = FE_{\mathrm{i}} \times \eta_{\mathrm{voltage,i}}(V_{\mathrm{OP}}) \tag{10}$$

For the prolonged operation under variable input, it is more practically meaningful to define $\eta_{EC,i}$ as the quotient of the total energy required for the production of a specific reaction product, i, to the total energy utilized by the EC cell over a given time interval. $E_{i,total}$ can be calculated as a product of total electric charge supplied to EC device and selectivity towards the product of interest, whilst E_{OP} is obtained by integrating the input electrical power at the operating points with respect to time.

$$\eta_{\mathrm{EC,\,i}} = \frac{E_{\mathrm{i,total}}}{E_{\mathrm{OP}}} \tag{11}$$

The energy required for the production of a specific reaction product, i, $E_{i,total}$ is given by

$$E_{\mathrm{i,total}} = E°_{\mathrm{i}} \times Q_{\mathrm{i}} \tag{12}$$

where $E°_i$ is the theoretical thermodynamic potential of product i, and Q_i is the amount of charge contributing to its formation. For gaseous products, the charge is expressed as the product of the EC cell current $I(t)$, the time of measurement t, and the Faradaic efficiency of product i, FE_i.

$$Q_{\text{gaseous products}} = I(t) \times t \times FE_{\mathrm{i}} \tag{13}$$

For $HCOO^-$, the charge is given by the product of Q_{total}, which is the integration of the current over the total experiment time interval when the liquid product is accumulated in the catholyte, and its Faradaic efficiency.

$$Q_{\mathrm{HCOO^-}} = Q_{\mathrm{total}} \times FE_{\mathrm{HCOO^-}} \tag{14}$$

Experimental uncertainties were estimated from instrument precision, calibration procedures, and repeated measurements where available, as presented in the dedicated section of the Supplementary Information.

Results and Discussion

The study has been carried out in three main experimental stages. First, the catalyst responsible for the formate production has been synthesized and thoroughly characterized. Then, the performance of the catalyst has been tested in the EC cell at different temperatures using standard electrochemical methods. Finally, the EC cell has been connected to the PV emulator and the main experimental study of the PV-EC operation in realistic conditions has been carried out. The results of the experiments are presented in this order below.

View Article Online
DOI: 10.1039/D6SE00442C

Characterization of Cu_2O:S cathode material

Sulfur-modified copper oxide nanopowder was synthesized based on research previously reported and adapted.[46,47] **Figure 3a** shows the XRD pattern of the Cu_2O:S catalyst, while **Figure 3b** and **c** show the SEM and EDX images after deposition on GDL substrate via airbrushing.

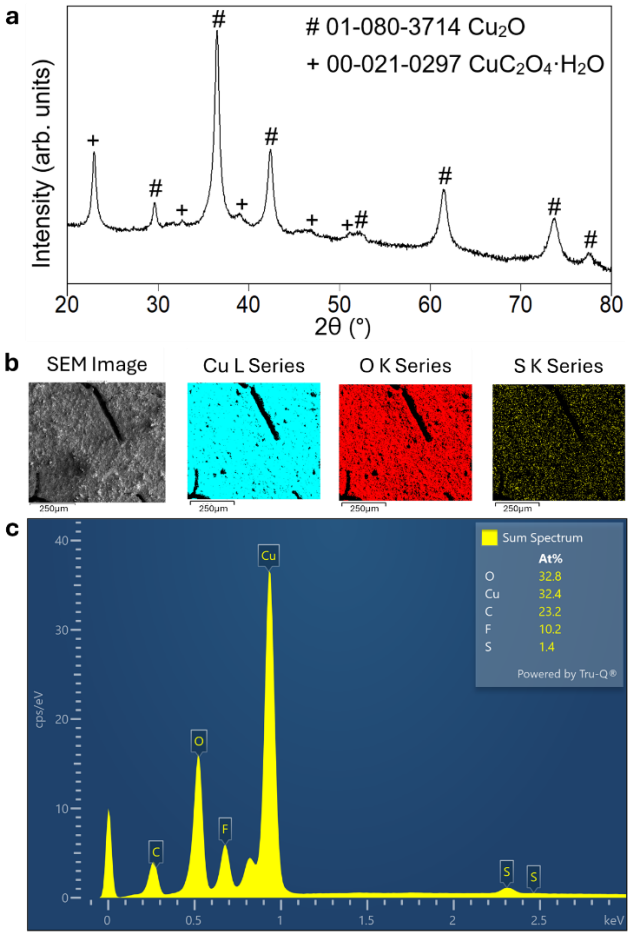

Figure 3. Characterization of Cu_2O:S cathode material. **a** X-ray diffraction (XRD) pattern of solvothermally synthesized Cu_2O:S nanopowder. **b** Scanning electron microscopy image (SEM) of Cu_2O:S/GDL electrode and corresponding elemental maps for Cu (cyan), O (red) and S (yellow) obtained by energy-dispersive X-ray spectroscopy (EDX). **c** Element distribution sum spectrum in atomic%.

The diffraction peaks marked with '#' with dominant reflections at 29.6° , 36.4° , 42.3° , 52.5° , 61.3° , 73.5° and 77.4° 2θ were detected, which correspond to the (110), (111), (200), (211), (220), (311) and (222) crystallographic planes of cubic copper(I) oxide (Cu_2O) with space group $Pn\bar{3}m$ (ICDD 01-080-3714).[48,49] Those marked with '+' correspond to a secondary phase copper oxalate monohydrate ($CuC_2O_4{\cdot}H_2O$). This phase is confirmed by its characteristic low-angle reflections, particularly around 22-23° and 31-32° 2θ which correspond to the (110) and (020) planes, respectively.[50,51]

View Article Online
DOI: 10.1039/D6SE00442C

EDX imaging show surface oxidation and the homogeneous distribution of sulfur particles across the geometric area of the GDE. The element distribution sum spectrum is as follows: oxygen (O) = 32.8 at.%, copper (Cu) = 32.4 at.%, carbon (C) = 23.2 at.%, fluorine (F) = 10.2 at.% and sulfur (S) = 1.4 at.%. Larger high-resolution images of the SEM and EDX images are shown in **Figures S5-6**.

The XRD pattern of the solvothermally synthesized nanopowder shown in **Figure 3a** indicates a mixed-phase material. The sharp and intense peaks, especially around ~36-38° and ~42° 2θ, demonstrate high crystallinity and confirm the selective formation of the Cu_2O phase, with no evident peaks attributable to metallic Cu or CuO. The higher-angle $CuC_2O_4{\cdot}H_2O$ phase peaks appear weak and overlapped, suggesting either low concentration or surface-associated residues. Given the starting materials (copper(II) nitrate salt) and solvent system (ethylene glycol), the formation of $CuC_2O_4{\cdot}H_2O$ is attributed to in-situ oxalate ion formation from the oxidative decomposition of ethylene glycol in the presence of Cu^{2+} ions under simultaneous reduction of nitrate to nitrous gases.[52–54] The oxalate ions then coordinate with Cu^{2+} and crystallizes as $CuC_2O_4{\cdot}H_2O$ during the cooling and washing steps. Overall, the XRD results confirm the successful synthesis of predominantly polycrystalline Cu_2O, with a small residual amount of $CuC_2O_4{\cdot}H_2O$ arising from polyol-mediated side reactions.

The EDX spectrum indicates that the synthesized material is primarily composed of a copper oxide phase (65.2 at.% total for Cu and O), and it also confirms the elemental composition of the fabricated GDE. The PTFE-line carbon-based GDL substrate and the Nafion binder used both contribute to the C and F elements detected. S is detected at a low level of 1.4 at.% and this is consistent with the synthesis conditions, where elemental S was added in a small molar amount (0.268 mmol S to 16 mmol Cu-salt, with an expected atomic ratio of sulfur S/(S+Cu) of 1.6 at.%). Although the Cu:O atomic ratio is close to unity, which nominally corresponds to a CuO phase, the absence of CuO reflections in the XRD pattern indicates that the bulk material is Cu_2O, with the EDX-derived O content likely due to surface oxidation which is evident in **Figure 3b**. The combined XRD-EDX analysis confirms the successful synthesis of a sulfur-modified copper oxide earth-abundant catalyst, which is the desired cathode material for controlled selectivity towards formate. These characterization methods, however, do not provide direct information regarding the chemical state of sulfur or its evolution under reaction conditions. More extensive characterization of similarly prepared sulfur-modified copper oxide catalysts performed before and after CO_2 reduction experiments can be found in literature.[46,47]

Temperature- and voltage-dependent electrochemical CO_2RR performance of Cu_2O:S/GDL cathode

Practical “low temperature” electrochemical reactors experience somewhat elevated operating temperatures due to the heat dissipation within the tightly packed stacks of the EC cells. In order to approach the practically relevant operating conditions, we study the influence of temperature on the CO_2 reduction reaction performance. This was assessed by recording linear sweep voltammetry (LSV) and chronoamperometry (CA) curves as well as the Faradaic efficiencies of the reaction products under different

View Article Online
DOI: 10.1039/D6SE00442C

temperatures. Quantification of the CO_2 reduction reaction products revealed the presence of formate ($HCOO^-$), hydrogen (H_2) and carbon monoxide (CO). **Figure 4a** and **4b** show the effect of the operating temperature on the EC product distribution as a function of temperature between 20 °C and 60 °C. The smallest contribution in the product mix had CO with partial current density increasing across the temperature range from 0 mA cm^{-2} to 1.4 mA cm^{-2} (no more than 6% of the total current density at its maximum). The Faradaic efficiency to CO (FE_{CO}) increases with increasing temperature up to 50 °C and decreases slightly by 0.6 percentage points at 60 °C. The next contributor in the product mix is H_2 with partial current density increasing monotonically across the temperature range from 1.4 mA cm^{-2} to 8.5 mA cm^{-2}, whilst H_2 selectivity increases similarly with increasing temperature from 12% to 32%. The dominating product of the CO_2 reduction reaction was formate, $HCOO^-$, with partial current density increasing from 9.7 mA cm^{-2} at room temperature to 16.9 mA cm^{-2} at 50 °C and little decrease by 0.4 mA cm^{-2} at 60 °C. The Faradaic efficiency to $HCOO^-$ (FE_{HCOO^-}) attains a maximum of 88% at 20 °C and decreases with increasing temperature steadily to 82% at 40 °C and more significantly to 63% at 60 °C.

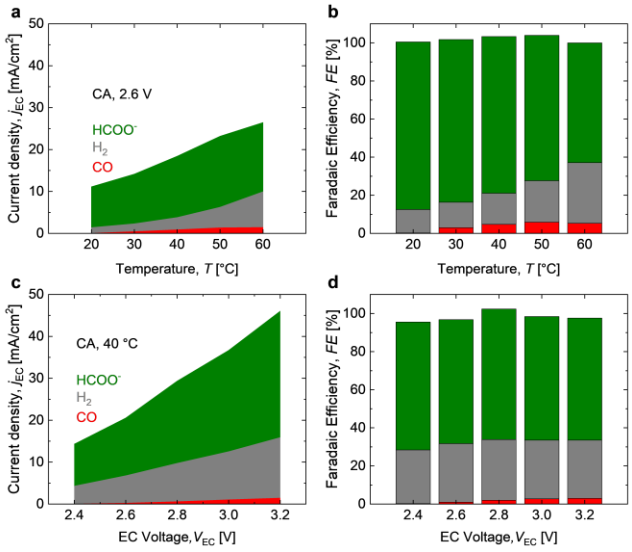

Figure 4. Partial current density and Faradaic efficiency towards the products obtained using Cu_2O:S/GDL cathode. **a** and **b** Temperature-dependent product distribution during 1 h CA at 2.6 V for each operating temperature. **c** and **d** Voltage-dependent product distribution during 1 h CA at each voltage at an operating temperature of 40 °C.

The results of the LSV and CA measurements are shown in **Figure 5**. It is observed therein that an increase in temperature from 20 °C to 60 °C increases the ionic conductivity of the electrolytes, both across the voltage range of 0 V to 4 V for the LSV and a time period of 1 h for the CA. The CA also shows that ionic conductivity increases over time more significantly as the operating temperature increases, with an 8% increase in EC current from 57 mA to 62 mA after a time period of 1 h at 20 °C and a 20% increase in EC current from 127 mA to 152 mA after the same time at 60 °C.

View Article Online
DOI: 10.1039/D6SE00442C

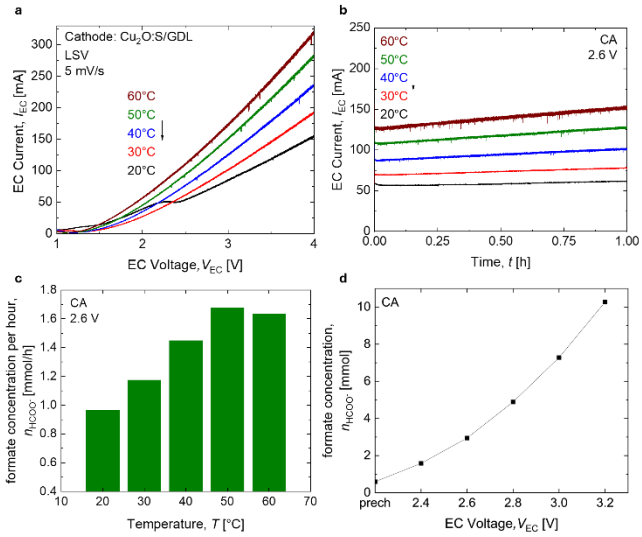

Figure 5. a Linear sweep voltammetry (LSV) and **b** chronoamperometry (CA) curves showing the effect of temperature on the cathode activity (EC current). Accumulated formate ($HCOO^-$) concentration **c** per hour during 1 h chronoamperometry (CA) at 2.6 V across the temperature range 20 °C to 60 °C, and **d** during CA at 40 °C in the same catholyte across the voltage range 2.4 V to 3.2 V. "prech" represents the concentration of accumulated $HCOO^-$ in the catholyte during the pre-characterization LSV.

The increase in EC cell current with increasing operating temperature as observed in **Figure 5a** is due to improved kinetics as the conductivity of aqueous electrolytes typically increase with temperature.[55] As the operating temperature increases, a decrease in CO_2 solubility is also expected.[55,56] With this decrease in CO_2 availability on the surface of the electrode, it is expected that the CO_2 reduction reactions are stalled. However, the CA curves in **Figure 5b** show an increase in the ionic conductivity of the electrolytes for the given applied voltage of 2.6 V over the 1 h time period at every operating temperature. This trend is typically not observed in a conventional water splitting or CO_2 reduction reaction (particularly to gaseous products). Instead, a stable or diminishing current is seen as the degradation of the cathode material occurs over time. Therefore, this characteristic could be associated with the production of $HCOO^-$ ions in the catholyte as shown in **Figure 5c**, its subsequent accumulation over time at the same temperature/in the same catholyte, and also its rate of production as it changes with temperature. These two scenarios have a direct impact on the ionic conductivity of the catholyte. Additionally, other factors such as the partial reduction of Cu(I) to Cu(0), improved wettability, exposure of additional active sites or changes in the local reaction environment could also enhance EC current during prolonged electrolysis, outweighing the effects of decreased CO_2 solubility. Therefore, the observed EC current trend is likely the result of a combination of formate accumulation and dynamic interfacial/electrode effects.

As the solubility of CO_2 decreases exponentially with increasing temperature, the competitive hydrogen evolution reaction (HER) is supported over the reduction of CO_2 to $HCOO^-$ as observed in literature.[57] An increase in operating temperature also increases the conductivity of the membrane which favors the HER

View Article Online
DOI: 10.1039/D6SE00442C

pathway due to more efficient proton transport from the anode to the cathode side.[57] This is reflected in the increase in both selectivity and activity to H_2. CO selectivity and activity also increase with increasing temperature; however, CO selectivity decreases slightly at 60 °C.

The slight decrease in $HCOO^-$ activity at 60 °C by 0.4 mA cm^{-2} to 16.5 mA cm^{-2} after consistent increase with increasing temperature could be due to the reduced rate of $HCOO^-$ production which influences the ionic conductivity of the catholyte. As shown in **Figure 5c**, $HCOO^-$ production follows the same trend as the current density and reduces from 1.67 mmol h^{-1} to 1.63 mmol h^{-1}. The decrease of $HCOO^-$ selectivity with increasing temperature is observed and could be concluded to be a trade-off as HER becomes more dominant. **Figure 5d** shows the accumulated formate ($HCOO^-$) concentration during the CA measurements at 40 °C in the same catholyte across the cell voltage range 2.4 V to 3.2 V. The term "prech" represents the concentration of accumulated $HCOO^-$ in the catholyte during the singular pre-characterization LSV performed at a scan rate of 5 mV s^{-1}.

Figure 4c and **d** show the effect of the applied voltage on the product distribution at 40 °C. Although FE_{HCOO^-} is observed to be maximum at 20 °C, operation at this temperature does not necessarily reflect realistic outdoor and upscaled PV-EC device conditions. While formate selectivity decreases moderately to 82% at 40 °C, the more pronounced drop to 63% at 60 °C indicates that higher temperatures shift selectivity to being more HER dominant. Therefore, an operating temperature of 40 °C was selected for subsequent experiments, balancing desired formate selectivity with realistic thermal conditions during targeted PV-EC device operation. The partial current density for CO, H_2 and $HCOO^-$ increase monotonically across the voltage range from 2.4 V to 3.2 V. An increase from 0 mA cm^{-2} to 1.4 mA cm^{-2} is observed for CO, from 4 mA cm^{-2} to 14 mA cm^{-2} for H_2 and from 10 mA cm^{-2} to 30 mA cm^{-2} for $HCOO^-$. In this case, because the CA measurements observed across the voltage range occur continuously using the same electrolyte, the accumulation of $HCOO^-$ ions improves the conductivity of the catholyte and overall current density. CO selectivity increases monotonically up to 3% at the maximum applied voltage of 3.2 V. H_2 selectivity is 28.2% at 2.4 V and is between 30.5% and 31.8% at the other applied voltages. $HCOO^-$ selectivity fluctuates between a low of 64% and peak of 68% across the applied voltage range of 2.4 V to 3.2 V.

Selectivity for H_2 was suppressed, with fluctuations characterized by a sample standard deviation of 1.35% observed across the voltage range. $HCOO^-$ selectivity being maintained between 64% and 68% and CO selectivity slightly increasing across the voltage range could be due to catalyst specific surface reactions.

$HCOO^-$ selectivity in electrochemical devices operated with copper (I) oxide cathode catalysts with 0.4 at.% and 0.45 at.% expected sulfur-modifications, respectively, have been shown to demonstrate increasing $HCOO^-$ selectivity with higher applied voltages (-0.4 to -1.0 V vs. RHE) and low-selectivity CO production at the highest operating voltages of -0.9 V vs. RHE and -1.0 V vs. RHE, respectively.[46,47] In this work, the expected atomic ratio of sulfur is 1.6 at.% and the influence of heteroatom doping with S on the enhanced product selectivity to $HCOO^-$ by suppressing or completely deactivating the CO path persists.

The same sequence of measurements was carried out using commercially purchased Sn nanopowder airbrushed on GDL substrate (Sn/GDL) as the cathode, fabricated similarly as previously described. The

View Article Online
DOI: 10.1039/D6SE00442C

results are shown in **Figure S7**. Similarly, with increasing operating temperatures, we observe a monotonical increase in H_2 selectivity up to 31.8% as HER is supported, whilst CO selectivity increases from 0.2% up to 5.9% at 50 °C before decreasing again slightly to 5.2% at 60 °C. However, as opposed to the relatively stable production of $HCOO^-$ across the applied voltages when utilizing the Cu_2O:S/GDL cathode, we observe a monotonical decrease in H_2 selectivity as $HCOO^-$ selectivity improves from 50.4% to 75.5% and CO selectivity remains relatively constant around ~14 - 16%.

Operation of direct-coupled PV-EC device under realistic dynamic irradiance and temperatures

The PV-EC device was operated according to the sizing parameters defined for the PV component as described above. The selected design point, marked by a golden star in **Figure 2c**, corresponds to a PV and EC cell-number ratio (η_{PV}/η_{EC}) of 4. Although a global maximum in solar-to-formate efficiency (STC_{HCOO^-}) is observed at a different ratio, marked by a green triangle, this point was not selected due to a lower PV-to-EC area ratio (A_{PV}/A_{EC}). Lower A_{PV}/A_{EC} results in less favorable operating conditions for power input and can restrict EC cell operation below the onset voltage, particularly under dynamic solar irradiance. Instead, the selected design point represents a deliberate trade-off between theoretical maximum performance for STC_{HCOO^-} and practical operability. It prioritizes robust PV power input without current-limited operation of the EC cell, yielding higher concentrations of the desired product. An integer η_{PV}/η_{EC} also enables a more straightforward modular upscaling using discrete cell stacks.

The PV-EC device was operated using an emulated 4-cell Si-based PV module with a total area of 10.35 cm^2 across the plane-of-array (POA) irradiance (G) and PV module temperature (T) combinations shown in the representative 24-hour condition set in **Figure S3**. The EC cell with a geometric area of 5.31 cm^2 was operated at 40 °C via heating of the electrolytes. The geometric area of the cathode is smaller than the nominal diameter of the GDE due to the coverage of its external diameter by the sealing gasket.

Figure 6 shows the scaled PV *I-V* curves of the emulated PV device across the defined G and T operating conditions. As the irradiance increases from sunrise to midday to a maximum value of 1055 W m^{-2}, the PV voltage output at MPP varies slightly by about 0.2 V, whilst the PV current output and power output increases more significantly. As the irradiance decreases from midday to sunset, the PV power output decreases.

View Article Online
DOI: 10.1039/D6SE00442C

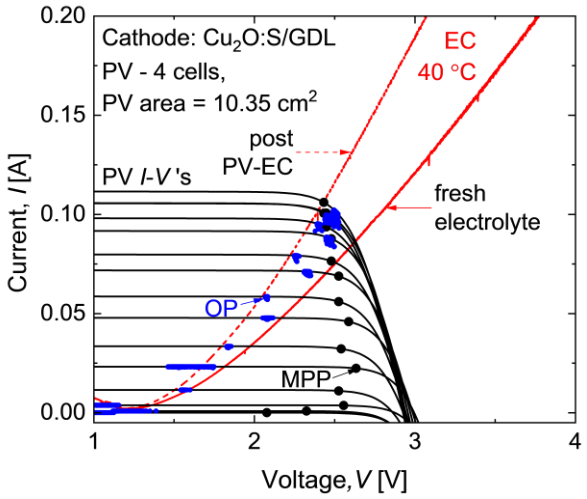

Figure 6. Polarization curves of the EC cell crossing the family of scaled PV module I-V curves. The black curves represent PV *I-V* characteristics at each irradiance and temperature, black markers denote the corresponding MPP points, blue markers denote the PV-EC operating points, and the red curves are the EC *I-V* polarization curves post PV-EC experiment and after a fresh electrolyte is used.

The polarization curves of the EC cell are measured via linear sweep voltammetry (LSV) over a voltage range of 0 - 4 V at a scan rate of 5 mV s^{-1}. The initial EC cell polarization curve was measured after the 6.8 h accelerated laboratory-timescale PV-EC experiment. The second polarization curve was measured after the EC cell was flushed of both electrolytes, replenished with fresh electrolytes, and re-stabilized at the operating temperature of 40 °C. Herein, we observe that the resulting *I-V* characteristics of the EC cell after the electrolytes were replenished closely reproduce those measured at the same operating temperature of 40 °C during the temperature-dependent electrochemical characterization of the EC cell between 20 °C and 60 °C. The PV-EC operating points, denoted by blue markers, also fall relatively within the limits of both EC cell polarization curves and aligns with the EC polarization curve used for PV sizing shown in **Figure 2a**. These observations are summarized in **Figure S8**.

During the operation of the PV-EC device, the EC cell polarization curve was measured twice in order to assess whether the PV-EC experiment altered the intrinsic electrochemical behavior of the EC cell. The initial polarization curve measured immediately after the 6.8 h accelerated PV-EC experiment reflects the condition of the EC cell after extended operation. Here, we observe an improvement in *I-V* characteristics due to the accumulation of $HCOO^-$ in the catholyte and possible dynamic interfacial/electrode effects. The second polarization curve was measured after flushing, replenishing and re-stabilizing both electrolytes at the operating temperature, and closely reproduces the previous measurements made during the electrochemical characterization of the EC cell as shown in **Figure S8a**. The PV-EC operating points lying within the limits of both polarization curves and matching the polarization curve used for PV sizing as shown in **Figure S8b**, confirms that the PV-EC device operated within the intended *I-V* range. It also indicates that the original EC polarization curve used for system design remains valid under real operating conditions.

View Article Online
DOI: 10.1039/D6SE00442C

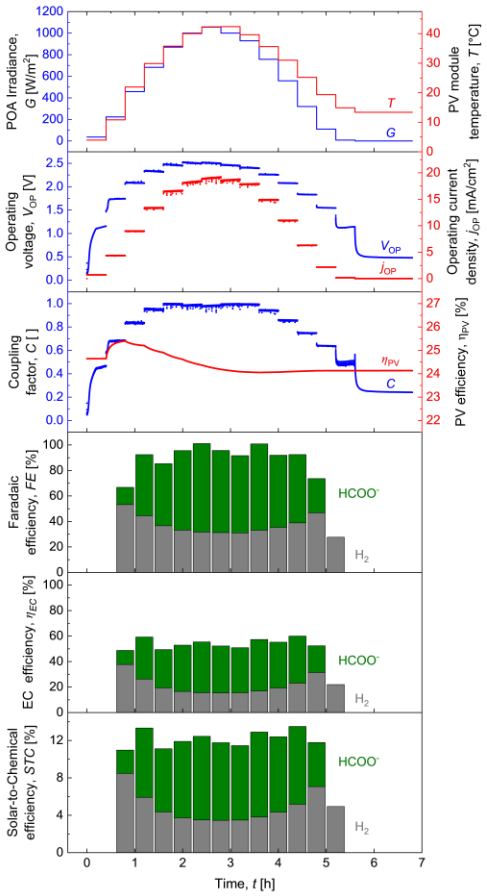

Figure 7. Input conditions and performance as a function of time for PV-EC device in realistic cycle at 40°C using Cu_2O:S/GDL cathode. The evolution of PV module irradiance and temperature, operating voltage and operating current density, coupling factor and PV efficiency, Faradaic efficiency, EC efficiency and solar-to-chemical efficiency with time are shown during accelerated laboratory-timescale PV-EC experiment.

Figure 7 displays the evolution of the input conditions (G, and T) as well as the performance of the PV-EC device via metrics previously defined (V_{OP}, j_{OP}, C, η_{PV}, FE, η_{EC}, and STC). The duration of operation stays within typical range of state-of-the-art reports for direct comparison. Both V_{OP} and I_{OP} followed trends similar to the irradiance (G), and the PV-EC power coupling factor (C) remained between 0.83 and 1 at significant irradiance levels (> 457 W m^{-2}) and for the majority of the operating period. At the maximum irradiances of 1 - 1.055 kW m^{-2}, the EC cell operated around 2.5 V, with C being between 0.98 and 1.

Within the first hour of the PV-EC experiment, G was around 200 W m^{-2}, corresponding to V_{OP} of approximately 1.74 V and EC cell operating current density (j_{OP}) of 4.4 mA cm^{-2}. Under these conditions, the total FE toward H_2 and $HCOO^-$ was ~67%, with H_2 being the dominant product (FE_{H2} = ~53%). As G and V_{OP} rise similarly across the realistic cycle, FE_{HCOO^-} increases from 13.5% to a maximum value of 69.4% at 1000 W m^{-2}, 2.49 V and 18.4 mA cm^{-2} on the upcycle, concurrently as FE_{H2} decreases to a minimum value of 27.6% at V_{OP} of 1.12 V and j_{OP} of 2.2 mA cm^{-2} on the downcycle. At maximum irradiance, both the

View Article Online
DOI: 10.1039/D6SE00442C

electrochemical efficiency for hydrogen production ($\eta_{EC,H2}$) and solar-to-hydrogen efficiency (STC_{H2}) reached their lowest values of 15.36% and 3.45%, respectively. In contrast, at G > 557 W m^{-2}, FE_{HCOO^-} ranged between 53 and 69%, corresponding to $\eta_{EC,HCOO^-}$ of 35.4 - 40.4% and STC_{HCOO^-} of 7.9 - 9.1%. CO was not detected by the GC within this range of EC operating current and voltage.

The predominant production of H_2 during the first hour of the experiment at an operating voltage of around 1.74 V is due to the HER being more kinetically favored over the CO_2 reduction. Moreover, this operating voltage is only ~0.31 V above the theoretical thermodynamic potential for $HCOO^-$ formation and therefore does not sufficiently account for the additional overpotentials attributed with the PV-EC device components for dominant production of $HCOO^-$. The trends in FE, η_{EC}, and STC inversely follow the curvature of the irradiance up- and downcycles, with higher selectivity, EC efficiency and solar-to-chemical efficiency towards $HCOO^-$ observed at higher irradiances. The lowest values of $\eta_{EC,H2}$ and STC_{H2} at maximum irradiance indicates suppression of the HER despite the highest available PV power output. Fluctuations in FE_{HCOO^-} are directly attributed to the detected concentrations by the IC. As irradiance decreases in the downcycle up to 110 W m^{-2}, $HCOO^-$ is no longer detected due to insufficient PV power input to overcome cathodic overpotentials and sustain the current densities required for CO_2 reduction. A PV-EC device energy coupling efficiency ($C_{PV\text{-}EC}$) of 94% was achieved, indicating highly effective transfer of PV energy to the EC cell.

Figure 8 shows the temporal evolution of energies associated with the PV-EC experiment. Energy evolution was determined by calculating the energy input from the PV device to the EC cell, and energy output into chemical products. The solar energy irradiated on the PV area was 3315 mWh and the energy at the MPP of the PV module was 800 mWh, namely the PV conversion efficiency (solar-to-electricity) was 24.1%. The energy at the OP was approximately 750 mWh, indicating a PV-EC energy coupling efficiency of 94%. The cumulative energy utilized to produce chemical products $HCOO^-$ and H_2 was 401.79 mWh, equating to an EC cell efficiency of 53.6%. Indicated are their respective total solar-to-chemical efficiencies, accounting for preferences for either CO_2 reduction or HER and operating point/power coupling mismatch as irradiance fluctuates during the realistic cycle. The largest part of the energy was lost due to overpotential losses of the EC cell represented by the voltage difference between the voltage at MPP and the voltage where the electrochemical reaction occurs. The PV-EC device achieved a total STC of 12.1%, with STC_{HCOO^-} of 7.9%.

View Article Online
DOI: 10.1039/D6SE00442C

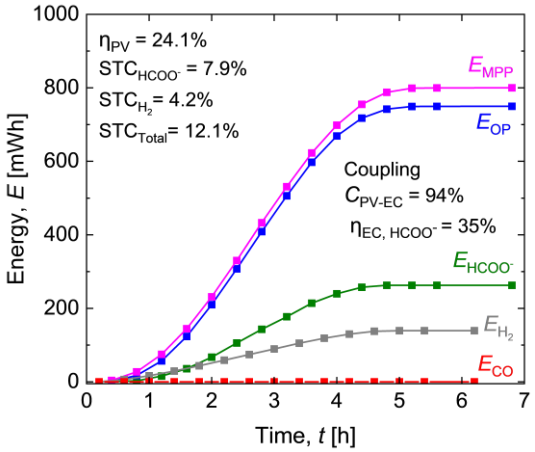

Figure 8. Energy evolution with time using Cu_2O:S/GDL cathode. E_{MPP} is the energy generated at maximum power point of the PV module. E_{OP} is the energy delivered to the EC cell. E_{H2}, E_{HCOO^-} and E_{CO} represent the energies utilized in the formation of each individual product. Comparing the energy profiles indicates the PV-EC device energy coupling efficiency (C_{PV-EC}) and the efficiency of the EC cell in terms of formate production ($\eta_{EC,HCOO^-}$). The calculated total *STC*s are also shown.

Figure 9 shows a direct correlation between PV-EC device efficiency (STC_{HCOO^-}) and electrochemical operating condition (j_{OP}). This allows for comparison between different electrochemical catalysts, cell designs or coupling strategies independent of absolute device area.

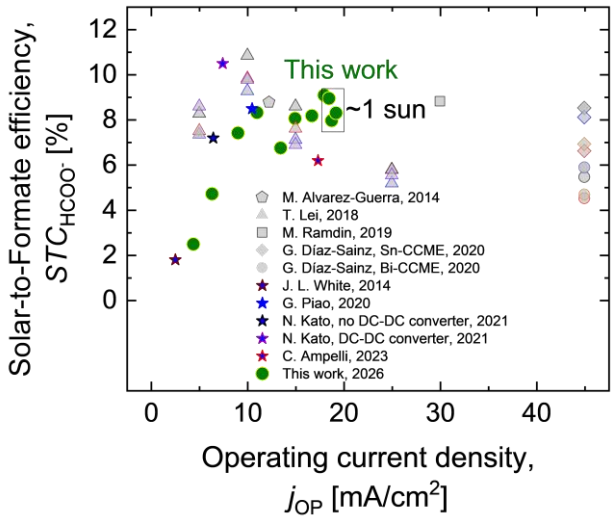

Figure 9. Comparison of solar-to-formate efficiency (STC_{HCOO^-}) as a function of operating current density reported for EC cells and PV-EC devices in literature. The greyed out icons are representative of experiments carried out using an EC cell, with approximations for solar-to-formate efficiency (STC_{HCOO^-}) in a direct coupled PV-EC device calculated using **Eq.** (6) and **Eq.** (10). The reported Faradaic efficiencies and operating voltages were taken into account, alongside an assumed PV efficiency of 24% and energy coupling efficiency of 1,

View Article Online
DOI: 10.1039/D6SE00442C

adopting optimal device coupling conditions with no energy losses due to mismatch. The blue stars, on the other hand, are representative of experiments carried out using a Si-based PV device coupled with an EC cell. The results of this study are depicted by green circles enclosed in yellow borders, showing single-point STC_{HCOO^-} across the operating current density range.

The grey pentagon with black borders is attributed to a EC cell where a Sn plate was employed as the cathode.[58] The grey triangles are attributed to experiments performed over current densities of 5, 10, 15 and 25 mA cm^{-2} using a Sn/GDE cathode. Grey triangles with purple, black, red and blue borders show results where a Nafion 117 cation exchange membrane and FAD, Yichen and A901 alkaline membranes were employed, respectively.[59] The grey square with black borders shows results for the application of a Sn-based cathode employed in a high pressure semi-continuous batch electrolyzer.[60] The grey diamonds with black, blue, orange and red borders shows results for the application of a Sn catalyst-coated membrane cathode used in a continuous filter cell at varying temperatures of 25 °C, 20 °C, 37.5 °C and 50 °C, respectively.[61] The grey circles with blue, black, orange and red borders shows results for the application of a Bi-based catalyst-coated membrane cathode at varying temperatures of 20 °C, 25 °C, 37.5 °C and 50 °C, respectively.[62]

The blue star with wine borders is attributed to experiments performed using an indium cathode in an integrated Si PV electrolyzer system, and represented the highest *STC* for solar CO_2 reduction at the time of publication (2014).[63] The blue star with blue borders shows results for the application of a porous Bi dendrites cathode and IrO_2 anode.[64] The blue stars with black and purple borders represent data from publications by N. Kato, in which a Ru-complex polymer cathode was utilized. The higher STC_{HCOO^-} was achieved in a system whereby a DC-DC converter with an efficiency of ~93% was employed. [65,66] The blue star with red borders shows results for the application of a similarly prepared sulfur-modified copper oxide cathode utilized alongside a mixed-metal oxide anode. A total *STC* of 10.1% was reported, with STC_{HCOO^-} of 6.2% and the rest towards H_2.[47]

The results of this study are depicted by green circles enclosed in yellow borders, showing relevant STC_{HCOO^-} in a broader current density range of 6 -19 mA cm^{-2} with PV-EC device operation under dynamic solar irradiance. This approach accounts for PV variability as a result of fluctuating weather and climate conditions, allowing for device performance evaluation relevant for field applications.

Conclusion

In our study, we demonstrated feasibility of the production of liquid solar fuels via the CO_2 reduction reaction in electrochemical cell directly coupled to PV module under realistic field operating cycle. This is achieved with combined application of a gas diffusion electrode (GDE) with an earth-abundant sulfur-modified copper oxide as catalyst in a flow electrochemical cell. The study progressed from the preparation and characterization of the catalyst material to characterization of the electrochemical device operating under variable temperatures, and finally to the testing of the electrochemical CO_2 reduction under the input from

View Article Online
DOI: 10.1039/D6SE00442C

a commercial PV module operating under field irradiance and temperature cycle. The accurate and reproducible operation of PV module and coupling to the small-scale experimental EC device was realized with high precision hardware PV emulator which can reproduce the required PV output under the target field scenarios.

In comparison with literature, this work shows a robust application of a direct coupled PV-EC device operating in a realistic cycle under dynamic solar irradiance, current densities and an elevated EC cell temperature of 40 °C. With the pair of a Cu_2O:S/GDL cathode and IrO_2/GDL anode, we demonstrate successful CO_2 reduction reaction with $HCOO^-$ as a main product, and H_2, as a byproduct with total Faradaic efficiencies > 92%. The performance of the PV-EC device transitions from being HER-dominated at solar irradiance below approx. 300 W m^{-2}, to being $HCOO^-$-dominated at higher irradiance. While $HCOO^-$ production was dominant at the highest energy generation regime, the PV-EC power coupling factor (*C*) stayed within the range of 0.83…1. An overall energy coupling efficiency of 94%, solar-to-formate efficiency (STC_{HCOO^-}) of 7.9% and total solar-to-chemical efficiency (*STC*) of 12.1% was achieved over the operating cycle. At the maximum current density of 19 mA cm^{-2}, single-point STC_{HCOO^-} reached 8.3% and total *STC* 11.7%. These values of STC_{HCOO^-} at the recorded current densities supersede previously published findings for comparable solar-driven CO_2 reduction setups. The initial *I-V* characteristics of the EC cell were maintained after 5.6 h of prolonged operation under variable solar irradiance conditions, and an additional 1.2 h in the dark. Although the stable catalytic performance observed suggests that the cathode catalyst remains structurally stable after prolonged operation, possible changes in the electrode structural or compositional state cannot be excluded. High overall energy coupling efficiency in the realistic operating cycle is owed to the optimized mutual sizing and power matching between PV and EC devices which was analyzed in dedicated simulation procedure and realized experimentally using flexibility of solar emulator. This demonstrates the feasibility of liquid-fuel production under realistic PV-driven direct-coupling operation, representing a key step toward early-stage long-term storage of surplus PV output in renewable-energy-dominated systems, and coupling of PV generation to non-electrified energy sectors.

View Article Online
DOI: 10.1039/D6SE00442C

Acknowledgements

The authors would like to thank Joachim Kirchhoff and Daniel Weigand for their technical assistance with the CO_2 reduction setup and gratefully acknowledge the European Commission under the SUPERVAL Project (Grant agreements no:101115456).

References

[1] G. Liu, D. McLaughlin, S. Thiele, C. Van Pham, "Correlating catalyst ink design and catalyst layer fabrication with electrochemical CO2 reduction performance" *Chemical Engineering Journal* **2023**, *460*, 141757.

[2] X. An, S. Li, X. Hao, Z. Xie, X. Du, Z. Wang, X. Hao, A. Abudula, G. Guan, "Common strategies for improving the performances of tin and bismuth-based catalysts in the electrocatalytic reduction of CO2 to formic acid/formate" *Renewable and Sustainable Energy Reviews* **2021**, *143*, 110952.

[3] H. Yang, Z. Xu, M. Fan, R. Gupta, R. B. Slimane, A. E. Bland, I. Wright, "Progress in carbon dioxide separation and capture: A review" *Journal of Environmental Sciences* **2008**, *20*, 14–27.

[4] M. Mikkelsen, M. Jørgensen, F. C. Krebs, "The teraton challenge. A review of fixation and transformation of carbon dioxide" *Energy Environ. Sci.* **2010**, *3*, 43–81.

[5] Y. Li, M. Sun, Y. Huang, Y. Wang, L. Ma, H. Yan, Y. Chen, "A Systematic Literature Review of Low-Carbon Technology Innovation: 2013–2022" *Energy Science & Engineering* **2025**, *13*, 2415–2427.

[6] L. M. Pastore, A. Sgaramella, G. Bruno, G. Lo Basso, L. de Santoli, "Coupling high-temperature electrolysis and industrial waste heat for on-site green hydrogen production: energy, economic and environmental analysis" *International Journal of Hydrogen Energy* **2025**, *126*, 87–98.

[7], "Global Energy Review 2025" **2025**.

[8] X. Xue, K. W. E. Cheng, C. Xu in *2024 10th International Conference on Power Electronics Systems and Applications (PESA)*, **2024**, pp. 1–9.

[9] M. Barman, P. Ravindran in *Photon to Power: Harvesting the Sun* (Eds.: P. Ravindran, D. K. G., A. Asok, D. Shankar, A.J. Ahmed), Springer Nature, Singapore, **2025**, pp. 393–406.

[10] M. Sheha, K. Mohammadi, K. Powell, "Solving the duck curve in a smart grid environment using a non-cooperative game theory and dynamic pricing profiles" *Energy Conversion and Management* **2020**, *220*, 113102.

[11] A. R. Dahiru, A. Vuokila, M. Huuhtanen, "Recent development in Power-to-X: Part I - A review on techno-economic analysis" *Journal of Energy Storage* **2022**, *56*, 105861.

[12] Q. Yan, J. Wang, T. Lin, A. J. Johnston, "Peak-Valley difference based pricing strategy and optimization for PV-storage electric vehicle charging stations through aggregators" *International Journal of Electrical Power & Energy Systems* **2025**, *169*, 110812.

[13] M. Hassanalieragh, T. Soyata, A. Nadeau, G. Sharma, "UR-SolarCap: An Open Source Intelligent Auto-Wakeup Solar Energy Harvesting System for Supercapacitor-Based Energy Buffering" *IEEE Access* **2016**, *4*, 542–557.

[14] B. P. Saripalli, G. Singh, S. Singh, "Supercapacitors based energy storage system for mitigating solar photovoltaic output power fluctuations" *World Journal of Engineering* **2022**, *20*, 815–834.

View Article Online
DOI: 10.1039/D6SE00442C

[15] J. Zhang, M. Gu, X. Chen, "Supercapacitors for renewable energy applications: A review" *Micro and Nano Engineering* **2023**, *21*, 100229.
[16] E. Villa-Avila, D. Ochoa-Correa, P. Arévalo-Cordero, F. Jurado, L. Sigüenza-Guzmán, "Real-time photovoltaic smoothing with supercapacitors: Low-complexity supervisory selection of conventional filters" *Electric Power Systems Research* **2026**, *254*, 112696.
[17] L.-C. Kin, A. Distler, O. Astakhov, B. Kone, H. Kungl, A. Karl, T. Merdzhanova, R.-A. Eichel, C. J. Brabec, U. Rau, "A matter of design and coupling: high indoor charging efficiencies with organic solar modules directly coupled to a sodium ion battery" *Journal of Materials Chemistry A* **2024**, *12*, 30862–30871.
[18] U. Chibuko, T. Merdzhanova, D. Weigand, F. Ezema, S. Agbo, U. Rau, O. Astakhov, "Module-level direct coupling in PV-battery power unit under realistic irradiance and load" *Solar Energy* **2023**, *249*, 233–241.
[19] S. Shcherbachenko, O. Astakhov, U. Chime, L.-C. Kin, K. Ding, B. Pieters, U. Rau, E. Figgemeier, T. Merdzhanova, "Efficient Power Coupling in Directly Connected Photovoltaic-Battery Module" *Solar RRL* **2023**, *7*, 2200857.
[20] F. Urbain, K. Wilken, V. Smirnov, O. Astakhov, A. Lambertz, J.-P. Becker, U. Rau, J. Ziegler, B. Kaiser, W. Jaegermann, F. Finger, "Development of Thin Film Amorphous Silicon Tandem Junction Based Photocathodes Providing High Open-Circuit Voltages for Hydrogen Production" *International Journal of Photoenergy* **2014**, *2014*, 249317.
[21] J. Jia, L. C. Seitz, J. D. Benck, Y. Huo, Y. Chen, J. W. D. Ng, T. Bilir, J. S. Harris, T. F. Jaramillo, "Solar water splitting by photovoltaic-electrolysis with a solar-to-hydrogen efficiency over 30%" *Nat Commun* **2016**, *7*, 13237.
[22] X. Zhou, R. Liu, K. Sun, Y. Chen, E. Verlage, S. A. Francis, N. S. Lewis, C. Xiang, "Solar-Driven Reduction of 1 atm of CO2 to Formate at 10% Energy-Conversion Efficiency by Use of a TiO2-Protected III–V Tandem Photoanode in Conjunction with a Bipolar Membrane and a Pd/C Cathode" *ACS Energy Lett.* **2016**, *1*, 764–770.
[23] H. Xiang, H. A. Miller, M. Bellini, H. Christensen, K. Scott, S. Rasul, E. H. Yu, "Production of formate by CO2 electrochemical reduction and its application in energy storage" *Sustainable Energy Fuels* **2019**, *4*, 277–284.
[24] O. Astakhov, S. N. Agbo, K. Welter, V. Smirnov, U. Rau, T. Merdzhanova, "Storage batteries in photovoltaic–electrochemical device for solar hydrogen production" *Journal of Power Sources* **2021**, *509*, 230367.
[25] F. Díaz-González, C. Chillón-Antón, M. Llonch-Masachs, S. Galceran-Arellano, J. Rull-Duran, J. Bergas-Jané, E. Bullich-Massagué, "A hybrid energy storage solution based on supercapacitors and batteries for the grid integration of utility scale photovoltaic plants" *Journal of Energy Storage* **2022**, *51*, 104446.
[26] X. Fang, X. Zhong, W. Dong, F. Zhang, Q. Yang, "Fuzzy logic-based coordinated operation strategy for an off-grid photovoltaic hydrogen production system with battery/supercapacitor hybrid energy storage" *International Journal of Hydrogen Energy* **2024**, *84*, 593–605.
[27] S. Rogowski, S. Hasan, A. Chub, M. Sibiński, "Enhancement of residential PV energy storage system by supercapacitor battery – high spatial resolution data analysis" *PEAS* **2025**, *74*, 269–280.
[28] K. B. Tawfiq, H. Zeineldin, A. Al-Durra, E. F. El-Sadaany, "Enhancing photovoltaic grid integration with hybrid energy storage and a novel three-phase ten-switch inverter for

View Article Online
DOI: 10.1039/D6SE00442C

superior power quality" *International Journal of Electrical Power & Energy Systems* **2025**, *167*, 110580.

[29] A. S. Agarwal, Y. Zhai, D. Hill, N. Sridhar, "The Electrochemical Reduction of Carbon Dioxide to Formate/Formic Acid: Engineering and Economic Feasibility" *ChemSusChem* **2011**, *4*, 1301–1310.

[30] M. Bevilacqua, J. Filippi, H. A. Miller, F. Vizza, "Recent Technological Progress in CO2 Electroreduction to Fuels and Energy Carriers in Aqueous Environments" *Energy Technology* **2015**, *3*, 197–210.

[31] E. Schuler, M. Morana, P. A. Ermolich, K. Lüschen, A. J. Greer, S. F. Rebecca Taylor, C. Hardacre, N. Raveendran Shiju, G.-J. M. Gruter, "Formate as a key intermediate in CO 2 utilization" *Green Chemistry* **2022**, *24*, 8227–8258.

[32] A. C. Lourenço, A. S. Reis-Machado, E. Fortunato, R. Martins, M. J. Mendes, "Sunlight-driven CO2-to-fuel conversion: Exploring thermal and electrical coupling between photovoltaic and electrochemical systems for optimum solar-methane production" *Materials Today Energy* **2020**, *17*, 100425.

[33] F. L. P. Veenstra, T. Cibaka, A. J. Martín, D. Weigand, J. Kirchhoff, V. Smirnov, T. Merdzhanova, J. Pérez-Ramírez, "CO2 Electroreduction To Syngas With Tunable Composition In An Artificial Leaf" *ChemSusChem* **2024**, *17*, e202301398.

[34] W.-H. Cheng, M. H. Richter, I. Sullivan, D. M. Larson, C. Xiang, B. S. Brunschwig, H. A. Atwater, "CO_2 Reduction to CO with 19% Efficiency in a Solar-Driven Gas Diffusion Electrode Flow Cell under Outdoor Solar Illumination" *ACS Energy Lett.* **2020**, *5*, 470–476.

[35] S. Wang, T. Kou, J. B. Varley, S. A. Akhade, S. E. Weitzner, S. E. Baker, E. B. Duoss, Y. Li, "Cu2O/CuS Nanocomposites Show Excellent Selectivity and Stability for Formate Generation via Electrochemical Reduction of Carbon Dioxide" *ACS Materials Lett.* **2021**, *3*, 100–109.

[36] Y. Chen, K. Chen, J. Fu, A. Yamaguchi, H. Li, H. Pan, J. Hu, M. Miyauchi, M. Liu, "Recent advances in the utilization of copper sulfide compounds for electrochemical CO2 reduction" *Nano Materials Science* **2020**, *2*, 235–247.

[37], "Controlled synthesis of copper sulfide-based catalysts for electrochemical reduction of CO2 to formic acid and beyond: a review" *Energy Advances* **2024**, *3*, 2704–2737.

[38] M. F. Seidler, B. Pieters, W. Zwaygardt, S. Haas, O. Astakhov, T. Merdzhanova, "A photovoltaics emulator for electrochemistry using Python and SCPI" *Journal of Power Sources* **2025**, *641*, 236723.

[39] U. Chibuko, T. Merdzhanova, S. Agbo, U. Rau, U. Wurstbauer, O. Astakhov, "Breaking limits of solar-to-hydrogen efficiency via synergy with batteries" *International Journal of Hydrogen Energy* **2025**, *127*, 38–50.

[40] T. Cibaka, T. Merdzhanova, O. Astakhov, S. Shcherbachenko, G. Liu, C. van Pham, U. Rau, P. Strasser, "Persistent CO2 Reduction Performance of an Ag Nanoparticle Gas Diffusion Electrode in Realistic Dynamic PV-Driven Operation" *Energy Fuels* **2025**, *39*, 22776–22783.

[41] O. Astakhov, T. Cibaka, L. Wieprecht, U. Rau, T. Merdzhanova, "Unfolding Electrolyzer Characteristics to Reveal Solar-to-Chemical Efficiency Potential: Rapid Analysis Method Bridging Electrochemistry and Photovoltaics" *ChemSusChem* **2025**, *18*, e202402027.

View Article Online
DOI: 10.1039/D6SE00442C

[42] A. Laudani, G. M. Lozito, F. Mancilla-David, F. Riganti-Fulginei, A. Salvini, "An improved method for SRC parameter estimation for the CEC PV module model" *Solar Energy* **2015**, *120*, 525–535.

[43] O. Astakhov, V. Smirnov, U. Rau, T. Merdzhanova, "Prediction of Limits of Solar-to-Hydrogen Efficiency from Polarization Curves of the Electrochemical Cells" *Solar RRL* **2022**, *6*, 2100783.

[44] L. Phan Van, L. Hieu Hoang, T. Nguyen Duc, "A comprehensive review of direct coupled photovoltaic-electrolyser system: Sizing techniques, operating strategies, research progress, current challenges, and future recommendations" *International Journal of Hydrogen Energy* **2023**, *48*, 25231–25249.

[45] M. T. Winkler, C. R. Cox, D. G. Nocera, T. Buonassisi, "Modeling integrated photovoltaic–electrochemical devices using steady-state equivalent circuits" *Proc. Natl. Acad. Sci. U.S.A.* **2013**, *110*, DOI 10.1073/pnas.1301532110.

[46] T. Shinagawa, G. O. Larrazábal, A. J. Martín, F. Krumeich, J. Pérez-Ramírez, "Sulfur-Modified Copper Catalysts for the Electrochemical Reduction of Carbon Dioxide to Formate" *ACS Catal.* **2018**, *8*, 837–844.

[47] C. Ampelli, D. Giusi, M. Miceli, T. Merdzhanova, V. Smirnov, U. Chime, O. Astakhov, A. J. Martín, F. L. P. Veenstra, F. A. G. Pineda, J. González-Cobos, M. García-Tecedor, S. Giménez, W. Jaegermann, G. Centi, J. Pérez-Ramírez, J. R. Galán-Mascarós, S. Perathoner, "An artificial leaf device built with earth-abundant materials for combined H2 production and storage as formate with efficiency > 10%" *Energy Environ. Sci.* **2023**, *16*, 1644–1661.

[48] N. H. Lam, N. Le, E. S. Kim, M. S. Tamboli, A. M. Tamboli, N. T. N. Truong, J. H. Jung, "Powder X-ray diffraction analysis of Cu/Cu2O nanocomposites synthesized by colloidal solution method" *Korean J. Chem. Eng.* **2022**, *39*, 2505–2512.

[49] N. H. Lam, R. P. Smith, N. Le, C. T. T. Thuy, M. S. Tamboli, A. M. Tamboli, S. Alshehri, M. M. Ghoneim, N. T. N. Truong, J. H. Jung, "Evaluation of the Structural Deviation of Cu/Cu2O Nanocomposite Using the X-ray Diffraction Analysis Methods" *Crystals* **2022**, *12*, 566.

[50] W. Kang, Q. Shen, "The shape-controlled synthesis and novel lithium storage mechanism of as-prepared CuC2O4·*x*H2O nanostructures" *Journal of Power Sources* **2013**, *238*, 203–209.

[51] C. Zhang, B. Zheng, Z. Song, S. Shi, H. Mao, "Microwave-assisted synthesis of a novel CuC2O4·xH2O/Graphene composite as anode material for lithium ion batteries" *Ceramics International* **2020**, *46*, 1018–1025.

[52] M. Stefănescu, V. Sasca, M. Bîrzescu, "Thermal behaviour of the homopolynuclear glyoxylate complex combinations with Cu(II) and Cr(III)" *Journal of Thermal Analysis and Calorimetry* **2003**, *72*, 515–524.

[53] M. Birzescu, M. Niculescu, R. Dumitru, P. Budrugeac, E. Segal, "Copper(II) oxalate obtained through the reaction of 1,2-ethanediol with Cu(NO3)2·3H2O" *J Therm Anal Calorim* **2008**, *94*, 297–303.

[54] J. Teichert, T. Doert, M. Ruck, "Mechanisms of the polyol reduction of copper(II) salts depending on the anion type and diol chain length" *Dalton Trans.* **2018**, *47*, 14085–14093.

[55] D. Ewis, M. Arsalan, M. Khaled, D. Pant, M. M. Ba-Abbad, A. Amhamed, M. H. El-Naas, "Electrochemical reduction of CO2 into formate/formic acid: A review of cell design and operation" *Separation and Purification Technology* **2023**, *316*, 123811.

View Article Online
DOI: 10.1039/D6SE00442C

[56] A. Löwe, C. Rieg, T. Hierlemann, N. Salas, D. Kopljar, N. Wagner, E. Klemm, "Influence of Temperature on the Performance of Gas Diffusion Electrodes in the CO2 Reduction Reaction" *ChemElectroChem* **2019**, *6*, 4497–4506.
[57] R. E. Vos, M. T. M. Koper, "The Effect of Temperature on the Cation-Promoted Electrochemical CO2 Reduction on Gold" *ChemElectroChem* **2022**, *9*, e202200239.
[58] M. Alvarez-Guerra, A. Del Castillo, A. Irabien, "Continuous electrochemical reduction of carbon dioxide into formate using a tin cathode: Comparison with lead cathode" *Chemical Engineering Research and Design* **2014**, *92*, 692–701.
[59] T. Lei, X. Zhang, J. Jung, Y. Cai, X. Hou, Q. Zhang, J. Qiao, "Continuous electroreduction of carbon dioxide to formate on Tin nanoelectrode using alkaline membrane cell configuration in aqueous medium" *Catalysis Today* **2018**, *318*, 32–38.
[60] M. Ramdin, A. R. T. Morrison, M. de Groen, R. van Haperen, R. de Kler, L. J. P. van den Broeke, J. P. M. Trusler, W. de Jong, T. J. H. Vlugt, "High Pressure Electrochemical Reduction of CO2 to Formic Acid/Formate: A Comparison between Bipolar Membranes and Cation Exchange Membranes" *Ind. Eng. Chem. Res.* **2019**, *58*, 1834–1847.
[61] G. Díaz-Sainz, M. Alvarez-Guerra, J. Solla-Gullón, L. García-Cruz, V. Montiel, A. Irabien, "Catalyst coated membrane electrodes for the gas phase CO2 electroreduction to formate" *Catalysis Today* **2020**, *346*, 58–64.
[62] G. Díaz-Sainz, M. Alvarez-Guerra, J. Solla-Gullón, Leticia García-Cruz, V. Montiel, A. Irabien, "Gas–liquid–solid reaction system for CO2 electroreduction to formate without using supporting electrolyte" *AIChE Journal* **2020**, *66*, e16299.
[63] J. L. White, J. T. Herb, J. J. Kaczur, P. W. Majsztrik, A. B. Bocarsly, "Photons to formate: Efficient electrochemical solar energy conversion via reduction of carbon dioxide" *Journal of CO2 Utilization* **2014**, *7*, 1–5.
[64] G. Piao, S. H. Yoon, D. S. Han, H. Park, "Ion-Enhanced Conversion of CO2 into Formate on Porous Dendritic Bismuth Electrodes with High Efficiency and Durability" *ChemSusChem* **2020**, *13*, 698–706.
[65] N. Kato, Y. Takeda, Y. Kawai, N. Nojiri, M. Shiozawa, S. Mizuno, K. Yamanaka, T. Morikawa, T. Hamaguchi, "Solar Fuel Production from CO2 Using a 1 m-Square-Sized Reactor with a Solar-to-Formate Conversion Efficiency of 10.5%" *ACS Sustainable Chem. Eng.* **2021**, *9*, 16031–16037.
[66] N. Kato, S. Mizuno, M. Shiozawa, N. Nojiri, Y. Kawai, K. Fukumoto, T. Morikawa, Y. Takeda, "A large-sized cell for solar-driven CO2 conversion with a solar-to-formate conversion efficiency of 7.2%" *Joule* **2021**, *5*, 687–705.

View Article Online
DOI: 10.1039/D6SE00442C

From sunlight to formate at realistic temperatures and dynamic irradiance: direct photovoltaic–electrochemical CO_2 reduction using a Cu_2O:S gas diffusion electrode

Ameerah Abioro[a], Oleksandr Astakhov[a], Sergey Schecherbanchenko[a], Claudio Ampelli[b], Daniele Giusi[b], Gabriele Centi[b], Siglinda Perathoner[b], Elmar Neumann[c], Yoo Jung Sohn[d], Christoph J. Brabec[a], Tsvetelina Merdzhanova[a]

[a] Ameerah Abioro, Oleksandr Astakhov, Sergey Schecherbanchenko, Christoph J. Brabec, Tsvetelina Merdzhanova
Institute of Energy Materials and Devices: Photovoltaics (IMD-3)
Forschungszentrum Jülich GmbH, 52425 Jülich, Germany
E-mail: t.merdzhanova@fz-juelich.de

[b] Claudio Ampelli, Daniele Giusi, Gabriele Centi, Siglinda Perathoner
Department of Chemical, Biological, Pharmaceutical and Environmental Sciences (ChiBioFarAm)
University of Messina, ERIC aisbl and CASPE/INSTM
Messina, Italy

[c] Elmar Neumann
Helmholtz Nano Facility (HNF)
Forschungszentrum Jülich, 52425 Jülich, Germany

[d] Yoo Jung Sohn
Institute of Energy Materials and Devices (IMD-2)
Forschungszentrum Jülich GmbH, 52425 Jülich, Germany

The data supporting this article have been included as part of the Supplementary Information and are available at https://fz-juelich.sciebo.de/s/adgRJd2A2okysoJ (password: cDEgSZSgsE).